Ore Geology Reviews 140 (2022) 104620

Contents lists available at ScienceDirect

Ore Geology Reviews

journal homepage: www.elsevier.com/locate/oregeorev

Extreme-resolution synchrotron X-Ray fluorescence mapping of ore samples

Mathis Warlo [a,*], Glenn Bark [a], Christina Wanhainen [a], Iris McElroy [b], Alexander Björling [c], Ulf Johansson [c]

[a] Division of Geosciences and Environmental Engineering, Luleå University of Technology, SE-971 87 Luleå, Sweden
[b] Boliden Mineral AB, SE-936 81 Boliden, Sweden
[c] MAX IV Laboratory, Lund University, SE-221 00 Lund, Sweden

ARTICLE INFO

Keywords:
Synchrotron
X-ray fluorescence mapping
Nanoscale
Trace metals
Gold
Rhenium
Bismuth
Molybdenite

ABSTRACT

In order to maximise profit and sustainability of a mining operation, knowledge of the chemistry, mineralogy, texture, and structure of the ore is essential. Continuous advancements in analytical techniques enable studying these features with increasing detail. Synchrotron radiation X-ray fluorescence is unparalleled in its simultaneously high spatial resolution and detection range. Yet, its application in ore geology research and the mining industry is still in its infancy. This study investigated opportunities of extreme-resolution synchrotron X-ray fluorescence mapping of ore samples. Analysis was performed at the NanoMAX beamline at the MAX IV synchrotron facility in Lund, Sweden. The samples investigated are from the Liikavaara Östra Cu-(W-Au) deposit, northern Sweden. Analysis covered areas of several hundreds of μm^2 in grains of molybdenite, pyrite, and native Bi. Key results included successful mapping of the lattice-bound distribution of Re, Se, and W in molybdenite at 200 nm spot/step size and detection of nanometre inclusions of Au in native Bi at 50 nm spot/step size. Challenges were encountered concerning data acquisition and processing. In order to achieve satisfactory resolution of both light and heavy elements and to limit mapping artefacts, repeated scans of the same area with varied experimental parameters and very thin (quasi-2d) samples are required. For complex geological samples, the software used for analysing spectral data (PyMCA) requires a considerable degree of human examination, which may be a source of error. Overall, synchrotron X-ray fluorescence mapping has a strong analytical potential for ore geology research, in analysing and imaging trace elements that would constitute potential by-products in mining operations. Detailed knowledge of how trace elements occur in the ores will inform the development of appropriate metal extraction programs thus ensuring that a larger part of the ore may then be utilized.

1. Introduction

Societal demand for metals and for their variety have strongly increased over the last few decades. Moreover, governmental organisations have identified certain metals as critical for society (e.g., U.S. National Research Council, 2008; European Commission, 2020). At the same time, sustainability in mining has become a growing public concern and environmental regulations for mining activities have become stricter in many countries (e.g., Eggert, 1994). These factors encourage more in-depth study of the often complex elemental composition of ore deposits. Some metals may be or become profitable to produce as by-products (e.g., Au and Ag), are harmful to the environment (e.g., As, U, Sb), or impede recovery of the main commodity (e.g., Bi in Cu), even in low concentrations. Furthermore, the mineralogy, association, character, texture, distribution, etc. of metals affect their behaviour during mineral processing and ultimately their recovery or suppression efficiency. Hence, detailed mineralogical and chemical knowledge of an ore body is crucial to maximise both profitability and sustainability of a mining operation.

For this task, the mining industry and ore geology research employ a number of micro-analytical techniques, in conjunction with traditional macro-analytical techniques and chemical assays. The micro-analytical techniques include scanning electron microscopy (SEM) coupled with energy dispersive spectrometry (EDS) and wavelength dispersive spectrometry (WDS), automated SEM-based techniques (e.g., QEMSCAN, MLA, Mineralogic, TIMA, AMICS, Inca-Mineral), electron probe microanalyzer (EPMA), secondary ion mass spectrometry (SIMS), laser ablation inductively coupled plasma mass spectrometry (LA-ICP-MS), X-ray fluorescence (XRF) based techniques (e.g., Bruker Tornado, CSIRO Maia Mapper, and Sigray AttoMap), laser induced breakdown spectroscopy

* Corresponding author.
E-mail address: mathis.warlo@ltu.se (M. Warlo).

https://doi.org/10.1016/j.oregeorev.2021.104620
Received 24 May 2021; Received in revised form 9 August 2021; Accepted 26 November 2021
Available online 30 November 2021

(LIBS), and more (Fig. 1). However, none of these techniques can achieve simultaneously as high a spatial resolution and detection range as synchrotron radiation X-ray fluorescence (SR-XRF; Stromberg et al., 2019, von der Heyden, 2020; Fig. 1). State-of-the-art synchrotron light sources provide spatial resolution down to 10 nm (Johansson et al., 2013, Stromberg et al., 2019) and sub-ppm detection levels (Smith, 1995; Adams et al., 2010, Stromberg et al., 2019; von der Heyden, 2020).

SR-XRF allows non-destructive chemical analyses of rock samples and can be combined with other synchrotron X-ray radiation techniques such as X-ray Absorption Fine Structure spectroscopy (XAFS) (e.g. Lintern et al., 2009; Majumdar et al., 2012). The use of synchrotron X-ray radiation has gained prominence in ore geology research over the last 10 to 15 years but is still largely under-utilized (von der Heyden, 2020). In the mining industry it has yet to find routine applications. Stromberg et al. (2019) mention the reasons for this under-utilization to be low availability, perceived high cost, and long data collection times, though these are being mitigated through advances in X-ray fluorescence detector technologies and X-ray optics. Additionally, the advent of fourth generation synchrotron light sources and its enhanced brilliance will likely further improve the affordance to scientists (von der Heyden, 2020). Several reviews on the application of synchrotron X-ray radiation in ore geology research have been published (e.g. Brugger et al., 2010; Cook et al., 2017; Stromberg et al., 2019, and von der Heyden, 2020). Cook et al. (2017) and von der Heyden (2020) outline one prominent field of application to be synchrotron X-ray fluorescence mapping (SR-XFM) to understand ore textures and chemical relationships at high (μm) spatial resolutions. Particularly, the pairing of SR-XFM with the Maia detector, which allows large area mapping (thin section size, typically 26 × 46 mm) at μm-resolution, has resulted in a number of publications (e.g. Ryan et al., 2013; Fisher et al., 2015; Li et al., 2016; Hu et al., 2016; Etschmann et al., 2017). In these publications, the focus is primarily on the detection level capabilities of SR-XFM, e.g. cm^2-scale trace element distribution mapping. In contrast, studies that test the potential of sub-μm spatial resolution, as this study does, are rare (e.g. Brugger et al., 2010).

Here, we present extreme-resolution (down to 50 nm spot size) SR-XFM data from two ore samples of the Liikavaara Östra Cu-(W-Au) deposit, northern Sweden. Analysis was performed at the state-of-the-art NanoMAX beamline at the MAX IV synchrotron facility in Lund, Sweden, and was the first ever analysis of ore samples at this beamline. The aim of the study was to explore opportunities for a possible industrial application of SR-XFM to aid in achieving more efficient and sustainable mining through detailed understanding of the trace element distribution in the ore. Emphasis was placed on the ability of SR-XFM to combine nanoscale spatial resolution with sub-ppm detection levels over square micron areas. The technique was used to study the distribution of impurities, both lattice-bound and as inclusions, in ore minerals. Impurities may affect the behaviour of ore minerals during processing or be of economic interest themselves. Hence, knowing in detail how these impurities occur, appropriate metal extraction programs can be developed, and recovery efficiency improved.

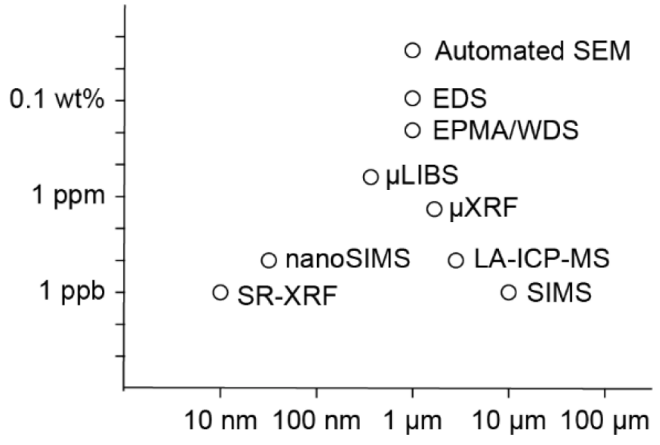

Fig. 1. Spatial resolution and detection limits of several analytical techniques commonly applied in ore geology research and the mining industry. SR-XFM exceeds the other methods in both aspect. The maximal spatial resolution aimed for in this study was 100 nm, corresponding to a spot/step size of 50 nm.

1.1. Mineralogical and metallurgical background of the study

The Liikavaara Östra Cu-(W-Au) deposit was chosen as a case study. Liikavaara Östra is a felsic intrusion-related vein-style deposit hosted by metamorphosed Paleoproterozoic volcaniclastic rocks. A detailed geological description of the deposit is presented by Zweifel (1976) and Warlo et al. (2020). The Liikavaara Östra Cu-(W-Au) deposit is scheduled for production by Boliden AB starting 2023. The ore contains 0.26 wt. % Cu with ppm-amounts of Au (0.06 g/t) and Ag (2.2 g/t). The Liikavaara ore will be blended into the production circuit of the nearby Aitik Cu-Au mine, where primarily Cu (0.4 wt. %) is produced with precious metals Au (0.2 g/t) and Ag (4 g/t) recovered as by-products from Cu-flotation. The precious metals mainly find application as jewellery and in investments. At Liikavaara Östra, Cu is hosted primarily in chalcopyrite within quartz veins and aplite dikes (Zweifel, 1976; Warlo et al., 2020). Analyses based on the SEM show Au to occur natively, in electrum and associated with native Bi, while Ag is observed in hessite (Ag2Te), Bi-Ag-tellurides, Ag-sulphides and electrum (Warlo et al., 2019; Warlo et al., 2020). The Au and Ag minerals are mainly hosted by quartz veins where they are found along grain boundaries of and as inclusions within sulphides (e.g. pyrite, pyrrhotite, chalcopyrite, sphalerite, and molybdenite) and as inclusions in quartz. Mineral grain sizes of Au are mainly below 10 μm and below 50 μm for the Ag-minerals (Warlo et al., 2020). The occurrence of fine-grained (<10 μm) Au and Ag locked in gangue minerals suggests at least some Au- and Ag-fraction of the ore to be refractory (Vaughan, 2004). Blending of ore in conjunction with the refractory nature of Au and Ag could prove challenging for efficient recovery of Au and Ag (Vaughan, 2004; Zhou & Cabri, 2004; Woodcock et al., 2007). Hence, a better understanding of their texture and chemical relationship may be beneficial to optimise the mineral processing (Harris, 1990; Coetzee et al., 2011). In this study, analysis of refractory Au by SR-XFM was tested as one possible field of application in the mining industry.

The Liikavaara Östra ore is enriched in Mo (31 g/t), which occurs as molybdenite, besides Cu and precious metals. This Mo concentration is similar to the Mo content in the Aitik ore (26 g/t). Wanhainen et al. (2014) suggest Mo as a potential future by-product of Cu-flotation based on a detailed study on the character and chemistry of molybdenite in the Aitik Cu-(Au) deposit and their implications for processing. The main use of Mo is in the production of alloys (Kropschot, 2009). Further, the mineral molybdenite finds application in lubricants and catalysts (Benavente et al., 2002; Kropschot, 2009). However, Benavente et al. (2002) suggest potential new applications of molybdenite in electronics, rechargeable batteries, and energy storage through intercalation with e.g., Li. Hence, production of Mo from the Liikavaara ore may also be profitable in the future. Nevertheless, recovery of Mo from Cu-flotation is generally more complex than that of Cu and subject to various mineral properties of molybdenite (Chander and Fuerstenau, 1972; Hoover, 1980; Dippenaar, 1982; Raghavan and Hsu, 1984; Ametov et al., 2008; Triffett et al., 2008; Zanin et al., 2008, Zanin et al., 2009; McClung, 2016). At Liikavaara Östra, molybdenite forms characteristically bent laths of ~ 0.2 mm and smaller. It is mainly found as aggregates or disseminated, often along the margins of quartz veins. Intergrowths with scheelite and other sulphides are occasionally observed (Warlo et al., 2020). Previous SEM-EDS studies of molybdenite revealed common micro-inclusions of Bi, Au, Ag, and Te (Warlo et al., 2020). However, observations were mostly limited to inclusions with a high brightness

contrast to the surrounding molybdenite in BSE (back-scattered electron) images. The suitability of SR-XFM to determine the variety and character of these micro- and nano-inclusions was tested in this study.

Molybdenite is not only the major source of Mo but also Re (Fleischer, 1959; Terada et al. 1971). Rhenium substitutes for Mo in the crystal lattice of molybdenite similarly to W (Frondel and Wickman, 1970; Pašava et al., 2016). Rhenium is an extremely rare but valuable metal used for high-temperature alloys and as a catalyst in chemical processes, and is mainly produced as a by-product from porphyry deposits (Millensifer et al., 2014). The Re content in molybdenite can vary significantly even within a single deposit but it rarely exceeds 1 wt% (Fleischer, 1959; Terada et al., 1971; Golden et al., 2013; Wanhainen et al., 2014; Millensifer et al., 2014; Pašava et al., 2016). For the Aitik ore an average of 211 ppm Re in molybdenite has been reported (Wanhainen et al., 2014). Despite these trace amounts, Wanhainen et al. (2014) suggest the possibility for profitable recovery of Re from the Aitik ore. This is largely attributed to the value Re adds to the recovery of Mo, which itself adds value to the primary Cu production. This exemplifies the idea of how a more holistic approach to mining may increase sustainability as well as profitability of a mining operation. The Re-content in the Liikavaara Östra ore is unknown, yet some substitution in molybdenite may be expected. A heterogeneous distribution of Re in single grains of molybdenite has been observed in some ore deposits (Aleinikoff et al., 2012; Ciobanu et al., 2013). In this study, SR-XFM was performed to detect a possible occurrence and distribution of Re in molybdenite.

2. Materials and methods

Two polished 30 μm-thin sections mounted on 1 mm-thick glass slides were prepared from two drill cores of the ore body of the Liikavaara Östra Cu-(W-Au) deposit. Three regions of interest (ROI) were selected based on petrographic microscopy (Nikon ECLIPSE E600 POL) and subsequent study by SEM-EDS (Zeiss Merlin FEG-SEM; Fig. 2):

(ROI-1) A molybdenite grain in a quartz-vein. The molybdenite grain has a lamellar texture and features several micro- to nanometre-thick cracks parallel to the lamellae.

(ROI-2) Micron-sized Au inclusions in subhedral pyrite grains in a quartz vein.

(ROI-3) A micron-sized native Bi grain with Au partitioning in a quartz vein.

After petrographic analysis (optical microscopy plus SEM-EDS), the thin sections were cut into 1x1 cm pieces with a manual glass cutter (scriber) to fit in the sample holder of the NanoMAX beamline at the MAX IV synchrotron facility in Lund, Sweden. Here, SR-XFM was performed. The beamline provides a hard X-ray monochromatic beam with a focal spot size of 50–200 nm. It is routinely operated at energies between 8 and 15 keV (5–28 keV possible). It is equipped with a RaySpec single-element silicon drift detector (SDD) coupled with an Xspress 3 (Quantum Detectors) pulse processor for XRF analysis. Analyses were performed at ambient conditions in the diffraction end-station, which allows a < 300 nm spatial resolution. A configuration of a 90° incident photon beam and 15° outgoing XRF beam was used. The ROIs for analysis were located with an optical in-line microscope. Petrographic and SEM-images of the samples at various magnifications aided alignment in the X-ray beam. For each scan, incident beam energy, pixel size, scan area, and dwell time were selected. In addition, the opening of a secondary source aperture (SSA) was adjusted for each scan to regulate the photon flux and control the X-ray count rate in the detector (Björling et al., 2020).

Post SR-XFM, SEM-EDS analyses (Zeiss Merlin FEG-SEM with Oxford Aztec software) were performed on selected spots to confirm some of the results of SR-XFM.

2.1. Analytical settings for SR-XFM

The experimental conditions were largely chosen to favour detection of heavy elements. Consequently, resolution of common mineral-forming light elements (e.g. Na, Mg, Al, and K) was not possible. Additionally, in the present setup Ar fluorescence from the air around the sample prevented adequate deconvolution of Ag emission lines. This was due to peak overlap between Ar-K and Ag-L emission lines. Incident beam energies used in this study ranged from 10 keV to 17 keV. The pixel size varied between 1000 nm and 50 nm and was mostly used to control scan time, i.e. large area scans were scanned at lower resolution

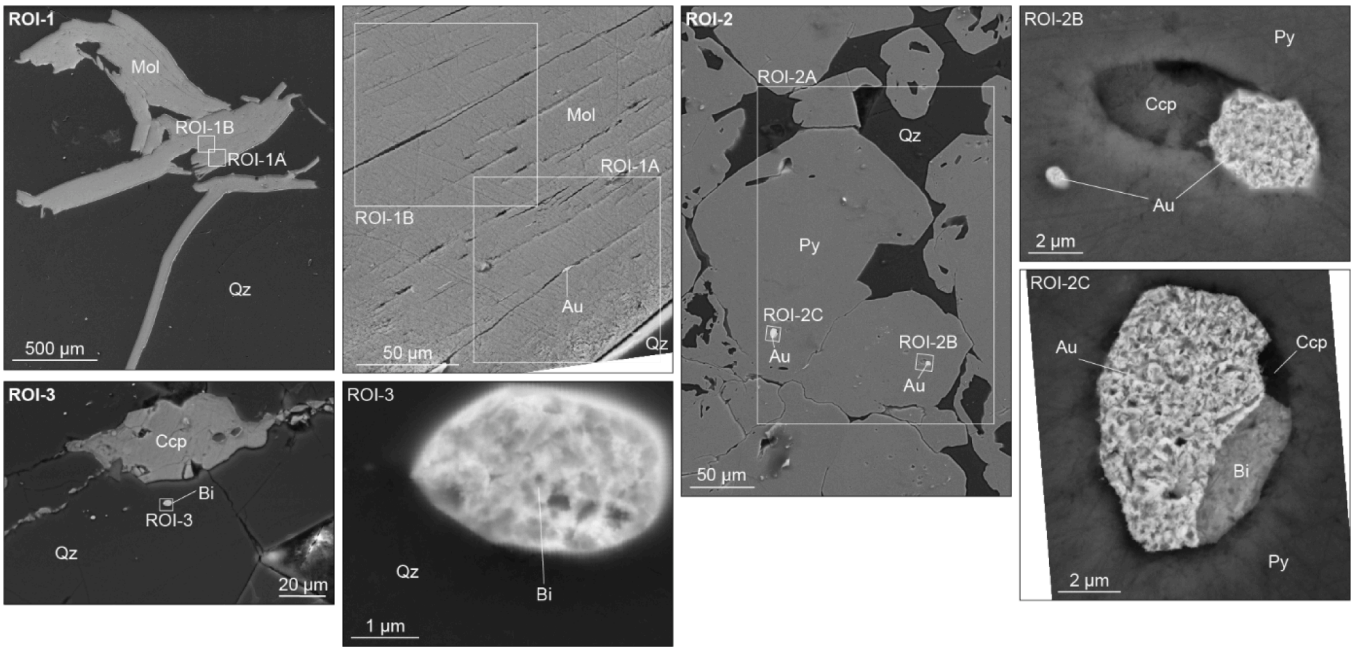

Fig. 2. Regions of interest selected for SR-XFM. (ROI-1) A molybdenite grain in a quartz vein. (ROI-2) Gold inclusions in a pyrite grain. (ROI-3) A droplet-shaped Bi grain in a quartz vein. Areas analysed by SR-XFM (white boxes) are shown at higher magnification to the right of each ROI.

compared to small area scans. Scan areas ranged between 180x270 μm to 5x4 μm. Dwell time was kept at 0.1 s for all scans. The experimental settings for each scan are summarised in Table 1.

At ROI-1 two elemental maps were collected (Fig. 2). The main goal was to detect and determine the element composition of inclusions and to image a potential distribution of lattice-bound impurities (Re, W, and Se) in molybdenite. The first map, ROI-1A, was 90x90 μm in size and centred on a Au inclusion (Fig. 2). It was stitched together from nine 30x30 μm scans with incident beam energies of 16 keV, pixel sizes of 500 nm and dwell times per pixel of 0.1 s. The photon energy of 16 keV was chosen above the absorption edge energies of some of the Bi-L lines. This was a trade-off between enabling Bi-excitation and managing photon flux and background fluorescence. The map was split into nine scans to mitigate time-waste in case of error. Completed scans could be processed and quality-checked so remaining scans could be halted and rerun if necessary. The second map, ROI-1B, was collected over a central part of the molybdenite grain (Fig. 2) in a single overnight scan of 90x90 μm with an incident beam energy of 15 keV, a pixel size of 200 nm and a dwell time per pixel of 0.1 s. The lower photon beam energy compared to ROI-1A was chosen to increase photon flux and the signal-to-noise ratio at the expense of excitation of the Bi-L lines.

At ROI-2 three elemental maps were collected to study a potential elemental zonation in pyrite and the element distribution within and around Au inclusions (Fig. 2). ROI-2A, a large-scale overview map of 180x270 μm over two pyrite grains, was stitched together from six scans of 90x90 μm. Incident beam energies of 16 keV, pixel sizes of 1 μm and dwell times per pixel of 0.1 s were used. Detector saturation occurred for the most intense Au and Bi inclusions but for all other areas the fluorescence signal was accurately acquired. ROI-2B covered a ~ 4 μm inclusion of Au, associated with chalcopyrite, in pyrite (Fig. 2). Another ~ 0.8 μm Au-grain in pyrite occurs next to this inclusion. Data were collected over an area of 12x10 μm with an incident beam energy of 17 keV (to excite all Bi L-lines), a pixel size of 100 nm and a dwell time of 0.1 s per pixel. ROI-2C covered a ~ 5 μm inclusion of Au, associated with native Bi and chalcopyrite, in pyrite (Fig. 2). It was collected over an area of 10x10 μm with settings equal to the previous scan.

At ROI-3 two elemental maps were collected to show element distribution over a Au-rich Bi grain in quartz (Fig. 2). The maps covered the same area of 5x4 μm but were scanned with an incident beam energy of 10 keV and 17 keV, respectively. The 17 keV scan was performed to excite elements past Zn-K and up to the Bi-L lines (e.g., Se-K, Au-L, Pb-L, and Bi-L). The 10 keV scan was performed to provide better signal-to-noise ratio for the lighter elements (~Ca-K to Zn-K). Pixel size (50 nm) and dwell time per pixel (0.1 s) were the same for both maps. But, actual resolution of the 10 keV scan was lower than of the 17 keV scan. This was due to the more open SSA, to the extent that it started broadening the focal spot (Björling et al., 2020), to increase the photon flux.

2.2. Processing of SR-XFM data

The detectors collected full spectral data, which were subsequently analysed using the PyMca software (Solé et al., 2007). A sum spectrum of each scan was calibrated to the detector set-up and conditions of the experiment. Background treatment was done via the SNIP-algorithm (Ryan et al., 1988). Peak fitting was performed with the Hypermet function on X-ray emission lines that were chosen based on prior knowledge on the composition of the samples, peak positions in the spectrum, and relative intensities between emission lines. Fixed relative intensities of X-ray emission lines from each element were used, and only the energy range from 1.5 keV up to 1 keV below the excitation energy was fitted. For quantification of the spectral data, the PyMca software allows either the fundamental parameters of the experiment (photon flux, detector active area, detector distance, and scan time) or a reference element from the matrix of the sample to be used as standard. Here, only pseudo-concentrations of the elements were calculated based on calibration to the same but arbitrary experimental parameters. This allowed qualitative comparison between data sets. From the fitted sum spectra software-generated fluorescence intensity maps of the individual element emission lines were produced. Based on these maps, spectral data of smaller regions within a map, e.g., from inclusions, were extracted and fitted. This was done to confirm occurrence of some elements and to search for other potentially occurring elements whose peaks may be 'drowned' in the sum spectrum of the whole scan.

During processing, some challenges with determining X-ray emission lines from the spectral data were encountered: (i) peaks of several lines overlapped. Broad peaks or visible 'shoulders' could indicate several emission lines, possibly of different elements, but certain identification was difficult. Additionally, peaks of elements with strong emission could entirely 'drown' peaks of elements with low emission. (ii) Fluorescence of elements with absorption edges far from the photon energy of the incident beam could barely exceed background levels. This was particularly true for trace elements. (iii) Different combinations of element emission lines achieved a visually similar calculated fit.

These challenges also had implications for the fluorescence maps: (i) fluorescence intensity distribution of comparably weak emissive lines spuriously mimicked that of overlapping, strong emissive lines. (ii) If emission was close to background levels, fluorescence intensity distribution could reflect the background rather than the emission line. (iii) Despite a visually similar fit of different combinations of element emission lines, the fluorescence map of the same emission line could vary between combinations.

Consequently, some ambiguity concerning the element composition of and distribution within a sample exists, and then especially for weakly emissive trace elements.

3. Results

3.1. Molybdenite (ROI-1)

SR-XFM of ROI-1A revealed most of the micro- and nanometre-cracks in molybdenite to be filled with impurities (Fig. 3). These impurities constitute mainly Fe-(Mn), Bi-(Pb-Se), and minor Cu-(Fe) (Fig. 3). Follow-up SEM-EDS analyses indicated Fe-phases to be both in the form of silicates and oxides. Other inclusions detected by SR-XFM, some not larger than one pixel (0.5 μm), contain Si, Ca, Au, Ag-Te, W, Ni, and Ti. A ~ 5x1 μm Au-(Ag) inclusion occurs in a crack in the centre of the scanned area and is associated with Bi-(Pb-Se) on both sides along the crack (Fig. 3). Broad Au-L peaks could indicate contribution from the L-lines of Pt and Hg. However, certain identification was not possible from the available data. The occurrence of Ag was mainly known from prior

Table 1
Analytical settings for SR-XFM (SSA - secondary source aperture).

Region of interest	Scan area [μm]	Pixel size [nm]	Incident beam energy [keV]	Dwell time [s]	SSA opening [μm]
1A (molybdenite)	90 × 90	500	16	0.1	26 × 15
1B (molybdenite)	90 × 90	200	15	0.1	26 × 15
2A (pyrite)	128 × 270	1000	16	0.1	26 × 15
2B (Au inclusion)	12 × 10	100	17	0.1	6 × 6
2C (Au inclusion)	10 × 10	100	17	0.1	6 × 6
3 (Bi grain)	5 × 4	50	17	0.1	6 × 7
	5 × 4	50	10	0.1	25.8 × 15.32

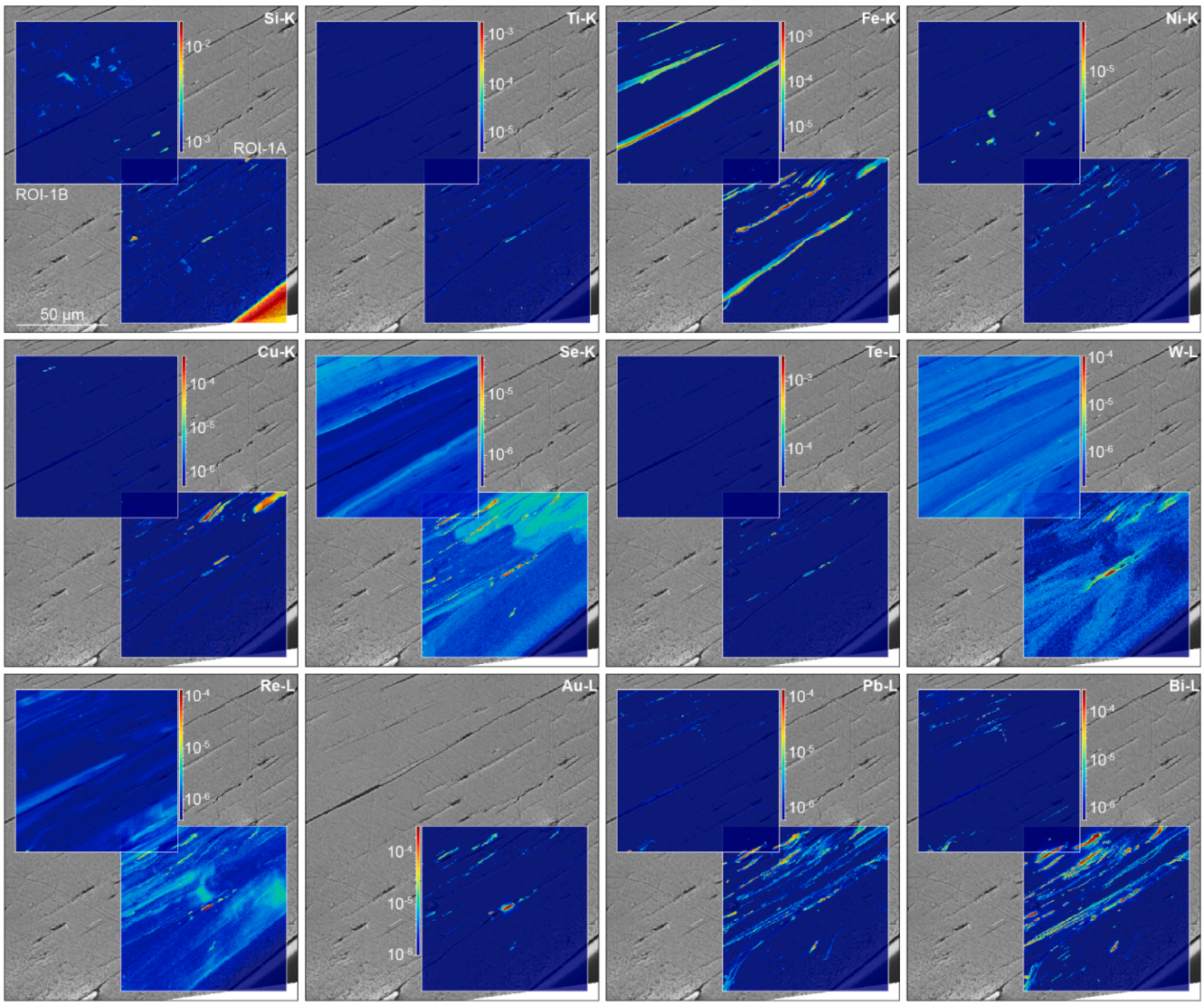

Fig. 3. Selected pseudo-quantitative SR-XFM element fluorescence maps of ROI-1. The scales are based on wt.% concentration but calibrated to an arbitrary set of values. This allows qualitative comparison between ROI-1A and ROI-1B. A logarithmic scale was used to better resolve weakly fluorescent features. A cut-off concentration was applied to all maps to separate features from background. Strongly fluorescent features mostly correlate to features visible in the underlying SE image. Weakly fluorescent features probably correlate to features deeper in the sample. Some features, e.g. the Au grain in the centre of ROI-1A, appear in several element maps. This is due to insufficient deconvolution of peak overlaps in the spectral data. However, in other cases this is due to a chemical association of several elements in the same mineral, e.g. Bi-(Pb-Se).

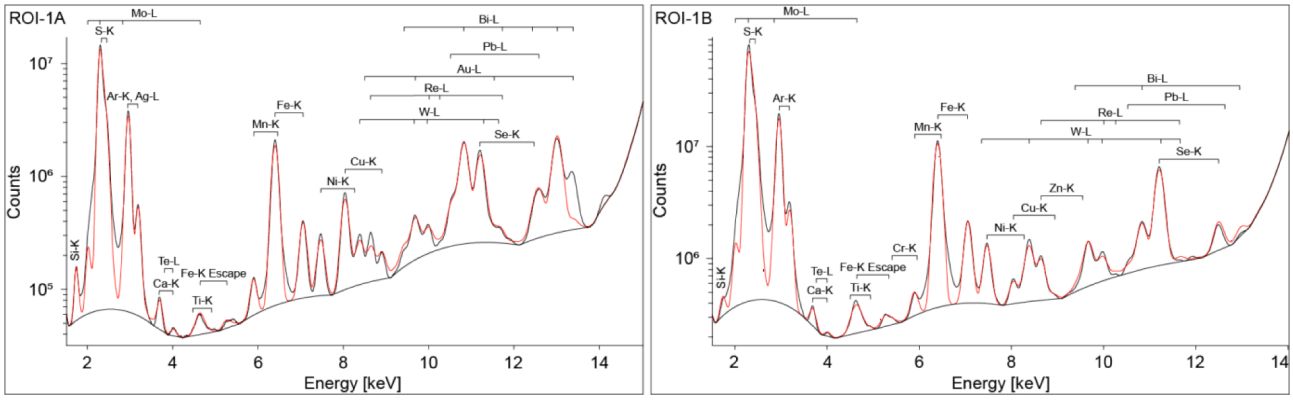

Fig. 4. SR-XFM sum spectral data for ROI-1A and ROI-1B. The fitted spectrum is marked in red. Background uses the SNIP algorithm (Ryan et al. 1988). Locations of fluorescence lines of elements used for fitting are shown.

SEM-EDS analyses. In the SR-XFM spectra, the Ag-L lines are mostly buried by Ar-K emission from the air in the beam path (Fig. 4). Nevertheless, Ag-L lines are observed in the spectral data of only the Au-(Ag) inclusion, indicating the occurrence of Ag together with Au, as is typically seen in ore mineralogy (electrum). Additionally, SEM-EDS spot analyses indicated several Ag-Te inclusions (signal mixed with molybdenite). In the SR-XFM spectra, fluorescence of Te is barely above background levels and additionally partly buried by emission from Ca (Fig. 4). Proper resolution of Te fluorescence would require a scan with lower incident beam energy. Yet, all Ag-Te grains identified with SEM-EDS were also resolved by SR-XFM and Ag- and Te-emission lines distinct in the respective spectra of these grains. Furthermore, on a logarithmic scale the SR-XFM maps show a large number of relatively weakly fluorescent inclusions of the above elements, which are not seen in the SE (secondary electron) and BSE images (Figs. 2 and 3). These inclusions are expected below the sample surface and only revealed by SR-XFM due to the higher excitation depth of the SR-XRF beam compared with the electron beam of a SEM.

SR-XFM also revealed a widespread distribution of Se, W, and Re in molybdenite, not linked to visible cracks and open spaces in the grain. The distribution of these metals is heterogeneous throughout the molybdenite grain (Fig. 3), with some lamellae in molybdenite showing strong and some weak fluorescence of Re, Se, and W. Abrupt as well as gradual changes in fluorescence occur. Individual fluorescence 'bands' range from micron to tens of micron width. Distinct changes in fluorescence across and diagonal to the lamellar texture occur. Additionally, the distribution of Re is inverse to that of W and Se. The latter two are largely similar. Peak overlap between the L-lines of W and Au, and Re and Au, respectively, result in a spurious strong fluorescence of W and Re in the central Au-inclusion (Figs. 3 and 4). SEM-EDS analyses failed to detect Re, Se, and W in molybdenite.

At ROI-1B the molybdenite grain contains fewer inclusions compared to ROI-1A. The inclusions are mainly Fe-(Mn), Si, Bi-(Pb-Se), Ni, some Cu, and few Zn, Cr, and Ti (Fig. 3). Especially the Fe-(Mn) inclusions seal elongated cracks. SEM-EDS spot analyses show Fe inclusions to be silicates. Some inclusions of Bi-(Pb-Se) are of only one to two pixel thickness, i.e. 200–400 nm (Fig. 3). Furthermore, Ti, Cr, and Zn occur as only a few pixels large spot-like inclusions. Their emission lines are distinct in the spectral data, when looking at the data from individual inclusions, but get lost in the total sum spectrum (Fig. 4). Many inclusions are not visible in the SE and BSE images (Figs. 2 and 3). They probably lie beneath the surface of the molybdenite grain.

Distribution of Re, Se, and W is generally similar to ROI-1A (Fig. 3). However, variation in fluorescence diagonal to the lamellar texture of molybdenite is almost absent. Also, spatial separation between Re and W, and Se is less pronounced (Fig. 3).

3.2. *Gold in pyrite (ROI-2)*

SR-XFM spectral data of ROI-2A suggests that pyrite contains As and possibly Co (Fig. 5). Confident identification of Co is difficult as the Co signal is dwarfed by the strong fluorescence of Fe in pyrite (Fig. 5). SEM-EDS spot analyses confirmed the occurrence of As, but not Co (possibly due to the EDS detection limits). However, the fitted fluorescence maps of Fe and Co are different, which supports an occurrence of Co. The pyrite grains are zoned with respect to Fe, As, and Co (Fig. 6). The distribution of As and Co is largely inverse to that of Fe, i.e. zones with strong As and Co fluorescence show weak Fe fluorescence and vice versa. In one pyrite grain, As fluorescence is strongest in the core, in another it surrounds a core of strong Fe fluorescence.

In some fluorescence maps (especially Fe), the grain boundaries of the pyrite grains show gradational decrease/increase in fluorescence towards the surrounding quartz (Fig. 6). This is caused by the beam excitation volume intersecting both pyrite and quartz at grain boundaries and is a result of the sample thickness (aspect ratio 1:60 compared with beam size) and the geometry of the experimental configuration

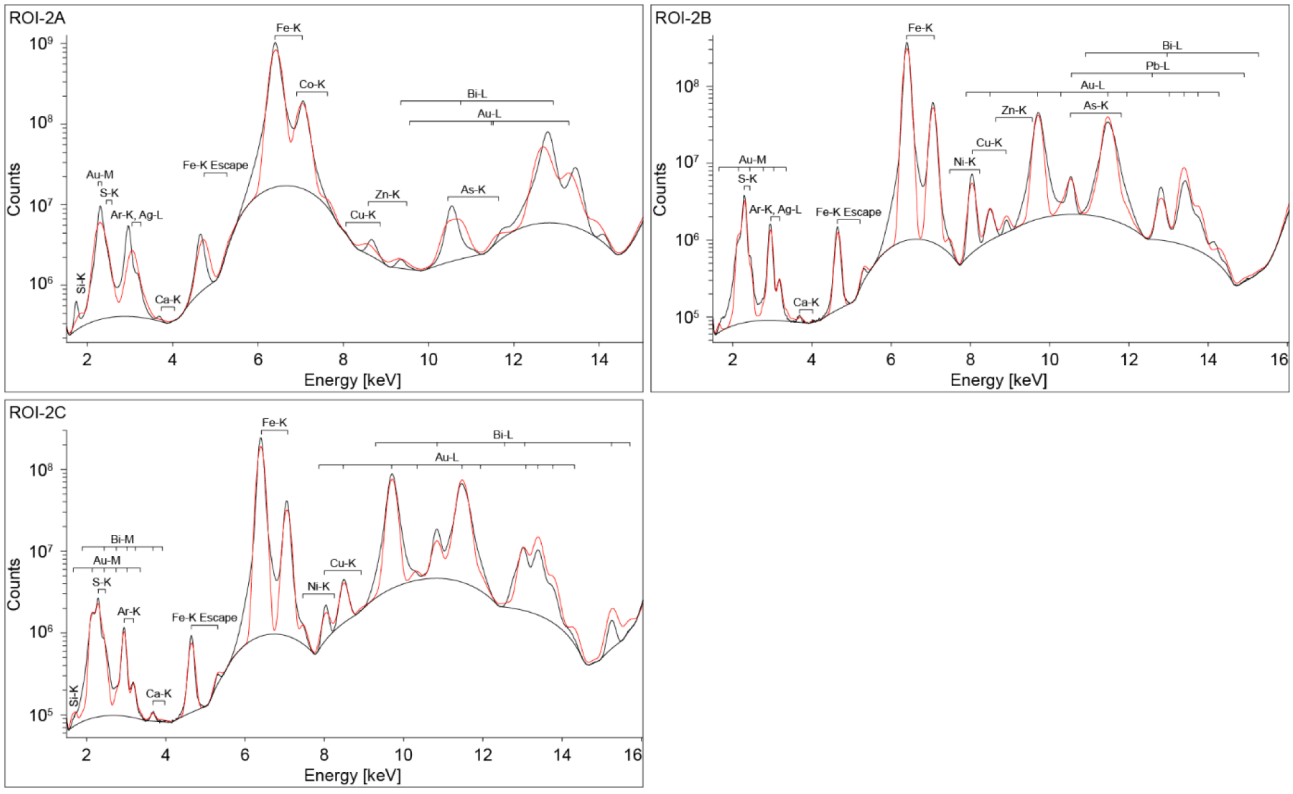

Fig. 5. SR-XFM sum spectral data for ROI-2. The fitted spectrum is marked in red. Background uses the SNIP algorithm (Ryan et al., 1988). Locations of fluorescence lines of elements used for fitting are shown.

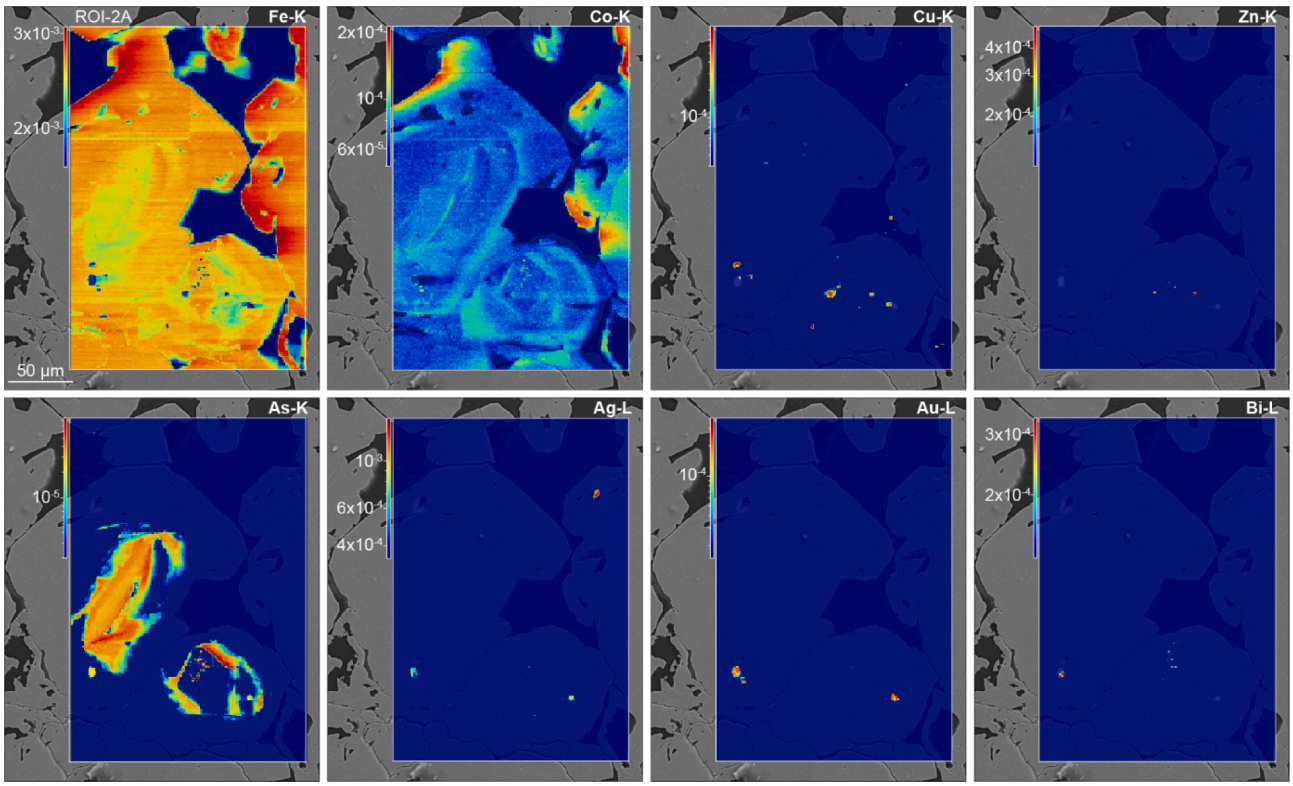

Fig. 6. Selected pseudo-quantitative SR-XFM element fluorescence maps of ROI-2A. The scales are based on wt.% concentration but calibrated to an arbitrary set of values. This allows qualitative comparison between element maps. A logarithmic scale was used to better resolve weakly fluorescent features. A cut-off concentration was applied to all maps to separate features from background.

(90° incident photon beam, 15° outgoing XRF beam).

The mapped pyrite grains contain several inclusions of Au, Bi, Cu, Zn, and Ag, which were subsequently confirmed by SEM-EDS (Fig. 6). Two ~ 5 µm Au grains are observed with a few submicron Au grains nearby. In one pyrite grain, the Au inclusion is associated with Bi (ROI-2C), and in another with Cu (ROI-2B). In the latter pyrite grain, Zn and Bi form an array of micron to sub-micron inclusions within the pyrite core. Copper forms several micron-sized inclusions in various pyrite grains and in quartz (Fig. 6). Optical microscopy and SEM-EDS analyses suggest these inclusions to be chalcopyrite.

At ROI-2B, the SR-XFM maps of Au and Cu show a gradual decrease in fluorescence from the core to the rims of the Au and chalcopyrite inclusions, respectively (Fig. 7). This spurious distribution pattern is again caused by the beam excitation volume intersecting adjacent minerals as the sample is thick compared to the beam size, with an aspect ratio of 1:300. Similarly, Fe and S fluorescence from pyrite is

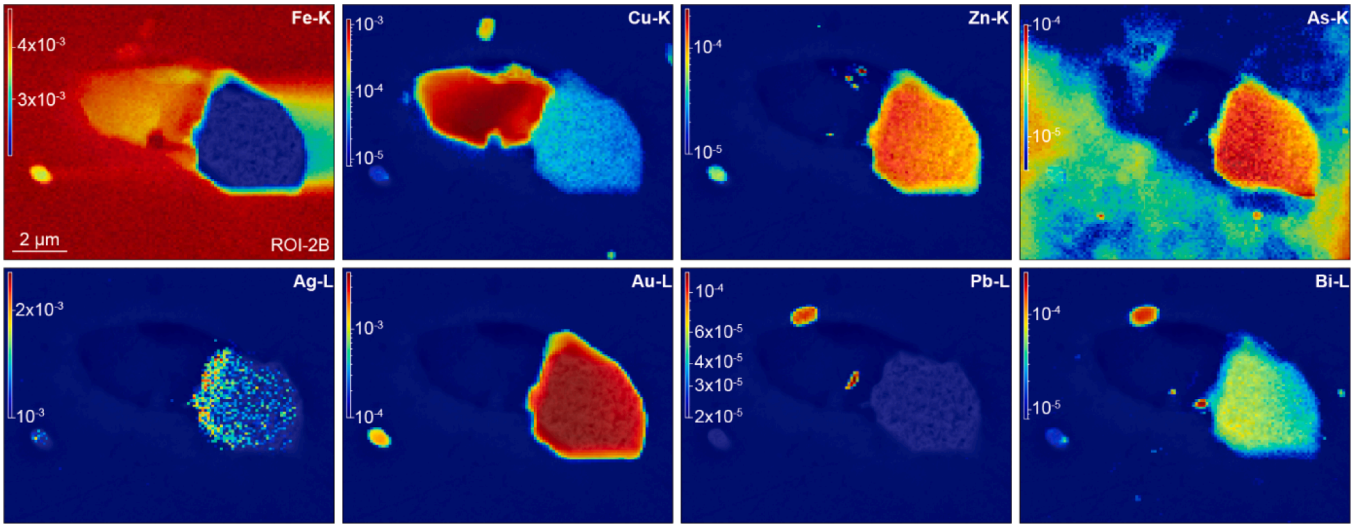

Fig. 7. Selected pseudo-quantitative SR-XFM element fluorescence maps of ROI-2B. The scales are based on wt.% concentration but calibrated to an arbitrary set of values. This allows qualitative comparison between element maps. A logarithmic scale was used to better resolve weakly fluorescent features. A cut-off concentration was applied to all maps to separate features from background. The Au grains appear in several element maps. This is mostly due to insufficient deconvolution of peak overlaps in the spectral data.

much weaker on one side of the Au inclusion than anywhere else in the grain. This 'shadow effect' is a result of the beam path configuration (90° incident photon beam, 15° outgoing XRF beam).

Other elements identified by SR-XFM are As, Bi, Pb, and Zn (Figs. 5 and 7). Arsenic fluorescence is strong in some areas within the pyrite grain. Bismuth, Pb, and Zn form nanometre inclusions within chalcopyrite and a 1 μm Bi-Pb grain is observed in pyrite close to chalcopyrite. Of these, only the Bi-inclusion in chalcopyrite is visible in the SE and BSE images (Figs. 2 and 7).

Many fluorescence maps (e.g., Cu, As, Bi, Pb, Zn) to some extent mimic maps of other elements (especially Au) (Fig. 7). This is spurious and caused by peak overlaps of the respective emission lines (Fig. 5). Only for Cu it is plausible that Cu fluorescence within the larger Au grain comes from chalcopyrite below the Au grain in the sample, although this is seemingly not reflected in the Fe fluorescence map (Fig. 7). In this case, the logarithmic colouring of the Fe fluorescence map is misleading, as the Fe signal from the Au grain (although present) is dwarfed by the Fe signal from the surrounding pyrite. In addition, the spectral data of the Au inclusion shows a shoulder on the peak of the Fe-Kβ emission line that is not visible in the total sum spectrum. This could indicate presence of Ni, but the resolution is insufficient to provide any certainty. Likewise, broad Au-L peaks could indicate the presence of Pt and Hg, but uncertainty is even higher compared with Ni. SEM-EDS spot analyses of the Au inclusion detected small portions of Ag and Fe. The Fe-signal came from the surrounding pyrite. Resolution of Ag by SR-XFM was not possible due to the overlap between Ar-K and Ag-L emission lines (Fig. 5). While the fluorescence map of Ag shows distribution within the Au grain, this could be due to overlap of the Ag-L and Au-M lines (Fig. 7).

SR-XFM of ROI-2C provided similar results as the SEM-EDS analyses had previously done. However, the Au fluorescence map indicates a Au grain in the corner of the analysed area, which is not visible in SE and BSE images (Figs. 2 and 8). It could possibly lie beneath the sample surface. This is supported by the weaker fluorescence of the Au grain in the corner compared to the Au grain in the centre of the map (Fig. 8). Similarly, the Bi and Cu fluorescence maps show a ~ 1 μm grain within the central Au grain and pyrite, respectively, which are not visible in the SE and BSE images (Figs. 2 and 8). Similar to ROI-2A and ROI-2B, intersections of multiple phases by the beam excitation volume and energy overlaps between emission peaks caused spurious patterns in most SR-XF maps (Fig. 8). The peaks of Fe-K, Au-L, and Bi-L are broad, but resolution is insufficient to separate possibly 'buried' emission lines of other elements, e.g., Mn-K, Pt-L, and Hg-L (Fig. 5).

3.3. Bismuth droplet in quartz (ROI-3)

Two scans (at 10 and 17 keV, respectively) cover the same Bi-inclusion with Au partitioning within quartz (Fig. 2). Yet, their respective spectral data and corresponding fluorescence maps show important differences (Figs. 9 and 10). The energy range up to 10 keV is much better resolved in the 10 keV scan (Fig. 9). This is particularly true for V, Cr, and Ti, whose K-emission lines hardly elevate from the background in the 17 keV scan (Fig. 9). Most fluorescence maps of the 10 keV scan show distinct nanometre inclusions of strong fluorescence within the Bi grain (Fig. 10). In contrast, 17 keV maps of the same elements largely fail to display these nanometre inclusions. Instead, their fluorescence patterns mimic that of Bi-L. However, the 17 keV scan allowed emission lines above 10 keV (Bi-L, Au-L, Pb-L, and Se-K) to be recorded. While it was possible to record Bi-M, Au-M, and Pb-M with the 10 keV scan, the corresponding fluorescence maps do not achieve the same level of detail as the L-emission line maps. Consequently, the results of the 10 keV scan are preferred for emission lines below 10 keV and the results of the 17 keV for emission lines above 10 keV.

The Bi grain contains three Au inclusions of 0.5–1.5 μm size (Fig. 10). Two of the inclusions lie centrally within the Bi grain, and the third occurs at the grain boundary of the Bi grain. A ~ 800 nm Fe-Mn inclusion and several sub-500 nm inclusions of Ni-Cr-Fe are also observed along the grain boundary (Fig. 10). Zinc, Ca, and Cu occur disseminated within the Bi-grain (Fig. 10). The Ca fluorescence may be caused by silicate inclusions in the Bi grain. Titanium and V are distinct in the spectral data, but their fluorescence maps mostly resemble the Bi-L emission pattern (Figs. 9 and 10). The Bi-L peaks are broad and suggest possible contribution from Pb-L and Se-L emission lines (Fig. 9). Fluorescence maps of Bi, Pb, and Se are similar, though this may be expected given the common mineralogical association of these three elements (Ciobanu et al., 2009; Fig. 10). Hence, occurrence of Pb and Se is inconclusive.

4. Discussion

4.1. Molybdenite

The results of this study imply widespread occurrence of micro- to nanometre-sized mineral inclusions of complex elemental composition in molybdenite at Liikavaara Östra. This is due to the layered texture of molybdenite, which allows substantial inclusion of foreign mineral grains in open spaces between layers (Ciobanu et al., 2013; Pašava et al., 2016; Ren et al., 2018). Understanding the character and occurrence of such impurities in molybdenite is mainly of interest for the study of ore forming processes. Impurities are also relevant for processing of molybdenite. Other studies have shown a decreased floatability of molybdenite due to silica inclusions and coatings with Ca, Fe, Mg, and K (e.g., Triffett et al., 2008; Zanin et al., 2009). Some of these elements were also observed as impurities in molybdenite in this study. Further, the occurrence of Bi and Pb impurities can lead to unexpected penalties at the smelter, and Au and Ag trapped in molybdenite decrease recovery of these previous metals. Considering the small amount of Au and Ag in

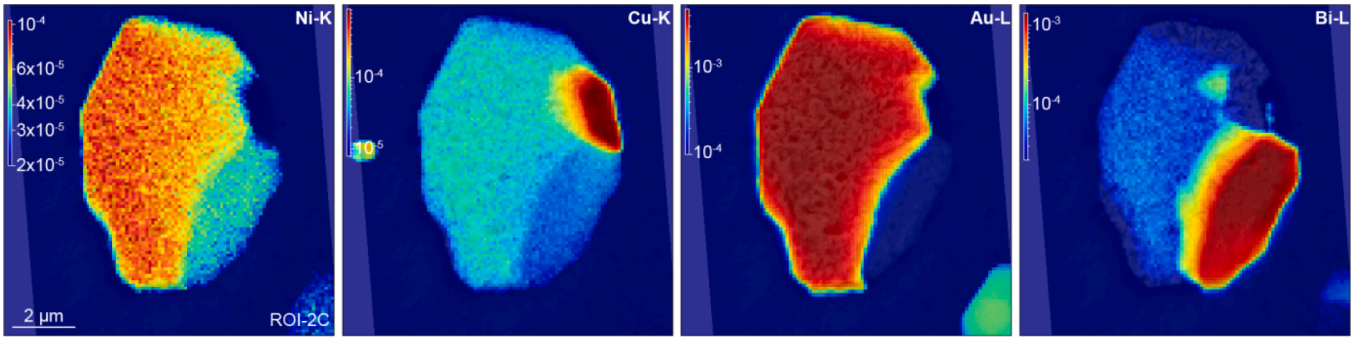

Fig. 8. Selected pseudo-quantitative SR-XFM element fluorescence maps of ROI-2C. The scales are based on wt.% concentration but calibrated to an arbitrary set of values. This allows qualitative comparison between element maps. A logarithmic scale was used to better resolve weakly fluorescent features. A cut-off concentration was applied to all maps to separate features from background. The Au and Bi grains appear in several element maps. This is mostly due to insufficient deconvolution of peak overlaps in the spectral data.

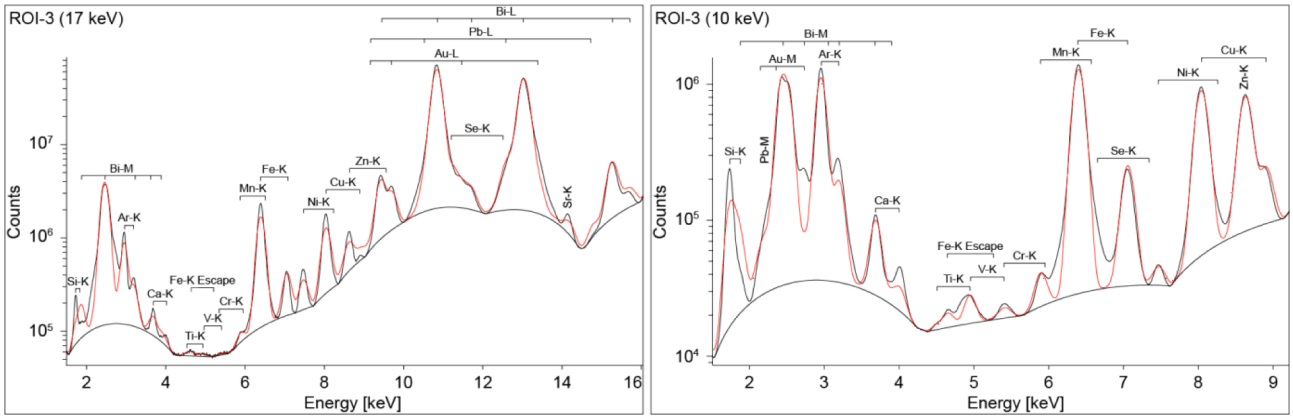

Fig. 9. SR-XFM sum spectral data for ROI-3. The fitted spectrum is marked in red. Background uses the SNIP algorithm (Ryan et al., 1988). Locations of fluorescence lines of elements used for fitting are shown.

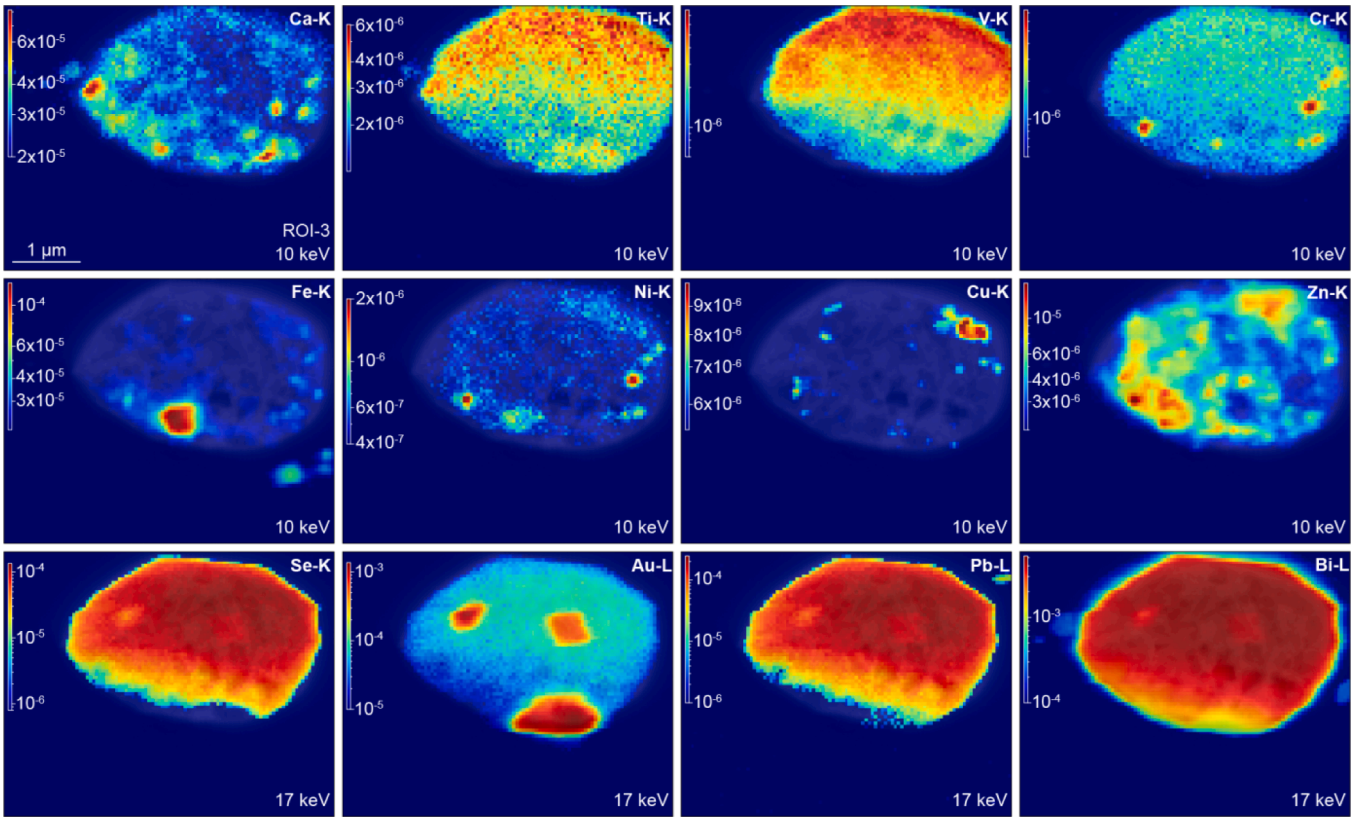

Fig. 10. Selected pseudo-quantitative SR-XFM element fluorescence maps of ROI-3. The scales are based on wt.% concentration but calibrated to an arbitrary set of values. This allows qualitative comparison between element maps. A logarithmic scale was used to better resolve weakly fluorescent features. A cut-off concentration was applied to all maps to separate features from background. Element fluorescence maps Ca-K to Zn-K are from the 10 keV scan, maps Se-K to Bi-L from the 17 keV scan.

molybdenite at Liikavaara Östra, their loss unlikely warrants the cost of additional steps to achieve recovery. Yet, it may be relevant for other deposits. To properly quantify a potential impact of impurities on processing of molybdenite requires a combination of micro- to nanoscale analyses with metallurgical tests of molybdenite from ore feed and concentrate.

SR-XFM revealed molybdenite at Liikavaara Östra to contain Re, W, and Se. This is relevant for a potential future production of Mo and Re from the blended ore of the Aitik and Liikavaara Östra deposits. Failure of SEM-EDS to adequately detect Re, W, and Se suggests their concentrations likely to be well below 1 wt%, which is common for these metals (Golden et al., 2013; Pašava et al., 2016). In comparison, Re in molybdenite of the Aitik deposit is on average 211 ppm, and still suggested to possibly be profitable (Wanhainen et al., 2014). If concentration at Liikavaara Östra was similar, this would further encourage production. The grain-wide distribution of Re, W, and Se suggests substitution for Mo (Re and W) and S (Se) in the crystal lattice of molybdenite, as described in the literature (e.g., Čech et al., 1973; Drábek, 1995; Frondel and Wickman, 1970; Pašava et al., 2016). However, an occurrence as nano-particulate inclusions below the resolution capability of the analyses cannot be excluded. Rhenium, W, and Se are heterogeneously distributed throughout the molybdenite grain (Fig. 3). In the literature,

heterogeneity of Re in molybdenite has been observed as oscillatory zoning, e.g. in the Hilltop deposit, USA (Ciobanu et al., 2013) and the Vosnesensk deposit, Russia (Grabezhev & Voudouris, 2014 and references therein). In addition, an inverse distribution of Re and W has been described for the Hilltop deposit, USA (Ciobanu et al., 2013). Furthermore, Terada et al. (1971) and Aleinikoff et al. (2012) described a core-rim relationship for Re in molybdenite grains from Japan and of the Hudson Highlands, southern New York, respectively. Results of this study confirm a largely inverse distribution of Re and W. However, the sub-micron spatial resolution (500 and 200 nm spot/step size, respectively) shows a much more complex pattern than simple oscillatory zoning (Fig. 3). A core-rim relationship cannot be inferred based on the obtained maps, although the scans did not cover an entire molybdenite grain. Comparison of SR-XFM with polarized light, SE, and BSE images fails to identify structures that may control the distribution of Re, W, and Se (Figs. 2 and 3). Dissolution/reprecipitation processes suggested by Aleinikoff et al. (2012) for molybdenite from the Hudson Highlands may have played a role also for the Liikavaara molybdenite, but further analyses are required. For processing of molybdenite and secondary Re recovery, the heterogeneous distribution of Re, W, and Se is mainly relevant in regard to determining their content in molybdenite. Spot-analyses, by e.g. LA-ICP-MS, will over- or underestimate the Re, W, and Se content, hence techniques analysing whole grains should be preferred when setting up a mineral processing scheme for the recovery of Re.

Molybdenite is a suitable mineral for absolute age dating, by making use of the ^{187}Re-^{187}Os isotopic ratio (Stein et al., 2001). Considering the likely Paleoproterozoic age of the mineralization at Liikavaara Östra (Warlo et al., 2020) some amount of radiogenic ^{187}Os should be expected (Stein et al., 2001). Yet, in this study, no Os was detected in the spectral data of the molybdenite scans. The most likely explanation is that the Os concentration was still too low to create sufficient fluorescence above background levels or that the SR-XFM map was done in an Os-poor part of the molybdenite grain. There is a possibility for decoupling of Re and Os, a mechanism first postulated by Stein et al. (1998, 2001). In this case, ^{187}Os is unlikely to be incorporated into the adjacent quartz (Stein et al., 2003) but should still be retained within other parts of the molybdenite grain. Stein et al. (2003) suggest radiogenic ^{187}Os to be stored in crystal defects such as kink bands and delamination cracks.

4.2. Gold in pyrite

Gold recovery from the Aitik processing plant is currently only coming from the Cu-flotation and the recovery rate < 50% (Sammelin et al., 2011). In a study on the Au mineralogy of the Aitik Cu-Au deposit, Sammelin et al. (2011) observed a significant amount of Au locked as fine inclusions in silicates and pyrite. They concluded this Au to be diverted to the tailings during Cu-flotation. Hence, in order to increase Au recovery other methods need to be employed. Cyanide leaching tested uneconomic due to low grade, low tonnage, and high cost of cyanide (Sammelin et al., 2011). Additionally, Sammelin et al. (2011) reported issues with cyanide consumption by sulphides and reduced cyanide effectivity on Au due to reaction with Ag. Nevertheless, leaching tests showed a 65% Au recovery through direct cyanide leaching and a 95% recovery by cyanide leaching on the residue (personal communications Nils-Johan Bolin, Boliden AB).

At the Liikavaara Östra Cu-(W-Au) deposit a similar distribution of Au compared to the Aitik Cu-Au deposit was observed (Warlo et al., 2020). While some Au occurs with chalcopyrite, a substantial amount is locked as very fine-grained inclusions (<10 μm) in quartz, pyrite and other gangue minerals (Warlo et al., 2020). The increased tonnage from blending of the Aitik ore with the Liikavaara Östra ore incentivises re-evaluation of cyanide leaching of the pyrite tailings. However, similar to Aitik (Sammelin et al., 2011), reduced cyanide effectivity on Au at Liikavaara Östra is expected. Many Au grains in the Liikavaara Östra ore contain a significant amount of Ag (Warlo et al., 2020) that may react with the cyanide solution and thereby generate lower Au recovery (Zhou & Cabri 2004). The Au in pyrite is partly associated with other sulphides (e.g., chalcopyrite), which leads to high cyanide consumption (Harris 1990). Furthermore, this study suggests a relationship between Au in pyrite and As-enrichment, though sample volume is insufficient to draw conclusions (Figs. 6 and 7). Yet, a link between refractory Au and As-enrichment has been described in many pyrite-bearing Au-deposits (e.g. Wells and Mullens, 1973; Fleet et al., 1989, 1993; Cook and Chryssoulis, 1990; Arehart et al., 1993; Craig et al., 1998; Pals et al., 2003; Belcher et al., 2004; Wu et al., 2019). In addition, this study showed several Bi- and other metal-inclusions associated with the Au-inclusions in pyrite. Hence, in a worst-case scenario, Au processing would require additional steps to remediate for As and Bi. On the other hand, the occurrence of Co, indicated though not confirmed by this study, yields the potential of another by-product. These uncertainties incentivise further mineralogical studies and metallurgical tests to extract Au (and Co) from pyrite in the Aitik processing plant.

4.3. Bismuth droplet in quartz

The occurrence of Au together with Bi-chalcogenides is common in ore deposits (Cook & Ciobanu, 2005; Cook et al., 2009). Experimental work (Douglas et al., 2000; Tooth et al., 2011), thermodynamic modelling (Wagner 2007, Tooth et al., 2008), and observations from ore deposits (Cook et al., 2009 and references therein) suggest Bi-melt to be the driving factor behind this association. Bi-melt may scavenge Au from aqueous fluids and subsequently crystalize if conditions are favourable (Liquid Bismuth Collector Model, Douglas et al. 2000). Mineralisation is typically observed as droplets of Bi-chalcogenides together with Au, within common ore minerals (Ciobanu & Cook, 2002). The occurrence of Au-containing Bi-droplets in quartz has been described for the Liikavaara Östra deposit (Warlo et al. 2020), and one such droplet was scanned by synchrotron XFM in this study (ROI-3), at a spot/step size of 50 nm.

SEM-EDS had previously shown the 3.5x2.3 μm large droplet to be mainly Bi with some partitioning of Au to one side of the grain. SR-XFM confirmed the occurrence of Au and revealed three distinct Au inclusions of 0.5–1.5 μm size (Fig. 10). This type of observation, Au inclusions in the Bi droplet, fits well with observations by Ciobanu et al. (2009), who interpreted irregular (spiky) time-resolved LA-ICP-MS data plots of Au across grains of Bi-chalcogenides as indications for nanoscale gold particles. Several other inclusions (Fe-Mn, Ni-Cr-Fe, Cu, Zn, and Ca) were observed by SR-XFM (Figs. 9 and 10). While Ciobanu et al. (2009) measured contents of Fe and Zn in Bi-chalcogenides with LA-ICP-MS, there is no mentioning on how these elements occur in the Bi grains. Results from SR-XFM in this study also suggest an occurrence of lattice-bound Pb and Se in the Bi grain. Both elements are common in Bi-tellurides (Ciobanu et al. 2009). In contrast, Cu, seen here disseminated across the grain with locally larger inclusions (Fig. 10), usually substitutes in Bi-sulfosalts (Ciobanu et al., 2009). Titanium and V, detected by SR-XFM, largely follow the Bi distribution (Fig. 10). It is unclear how these elements are related to the Bi grain. Some impurities like Ca, Fe, and Mn may point to minute silicate inclusions within the Bi grain. Overall, although only one Bi-droplet was scanned by SR-XFM, the results suggest the composition of these droplets to be more complicated than indicated by the available literature. This motivates further ore genetic studies to understand the formation of these complex phases.

With respect to the recovery of Au in the mineral processing, the Bi-droplets are troublesome. They are distributed in gangue (quartz), are only a few micrometre large, and carry Au, which additionally is partially locked within the grain. Gold in these Bi-droplets is therefore lost to the tailings during processing, so the proportion of Bi/Au droplets in the ore needs to be investigated properly.

4.4. Challenges of SR-XFM of ore samples

While SR-XFM analyses provided highly detailed and interesting results, this study also revealed challenges concerning analysis and data processing of SR-XFM of ore samples.

The unique construction of each synchrotron facility provides a large variety of analytical set-ups. While this is a key benefit over lab-based systems, it also means considerable time needs to be spent on the planning of an experiment in order to choose a suitable beamline and to maximise the output. Synchrotron radiation is highly customisable to individual needs. Various parameters like photon energy, photon flux, dwell time, pixel size, etc. have to be carefully selected to collect quality data and minimise image artefacts. Superior brilliance and extreme spatial resolution of synchrotron radiation allows collection of large amounts of data in a rather short time frame. However, for optimal results, several scans with variable experimental set-up and analytical settings are sometimes necessary.

In this study, Ar fluorescence from the air in the beam path prevented adequate resolution of Ag fluorescence. High-energy scans necessary to excite L-emission of heavier metals like Au and Bi were much poorer in the resolution of lighter elements compared to low-energy scans. This was clearly shown by the analyses of a Bi grain at 17 keV and 10 keV, respectively (Fig. 9). The setup of a 90° incident beam produced a large beam interaction volume in the samples and consequently high flux. Particularly at grain boundaries, this caused the interaction volume to intersect adjacent phases resulting in mixed fluorescence. This was seen as variations in fluorescence intensity in some fluorescence maps. For example, in the Au inclusions in pyrite, variations in Au fluorescence due to mixed fluorescence overlaid any potential chemical variations within the grains. Thus, the benefit of the 100 nm spot/step size was somewhat negated and information largely similar to that obtained by SEM-EDS.

These issues may be addressed by: (i) use of a vacuum chamber or simpler He tent to remove Ar fluorescence, (ii) variable incident beam energies to properly resolve light and heavy elements, (iii) polishing the sample to quasi-2d (e.g., by focused ion beam milling) to reduce the beam interaction volume, or (iv) use of a 3d technique (x-ray fluorescence tomography) to adequately resolve the sample depth. However, these 'fixes' have to be weighed against the limited beam time.

The software used for analysing SR-XFM (PyMCA) data can handle most varying experimental conditions and types of samples. This adaptability in the software necessitates expert skills of the user. In ease-of-use and automation it trails behind counterparts for lab-based systems. However, when a first set of analysis parameters has been established, further analyses can be automated. It should be noted, though, that for accurate quantification of several elements, with widely spanning concentration levels, a human examination is often needed. With the complex geological samples, this is the case. Here, peak-overlaps, broad peaks, and near-background peaks made assessment of the presence or absence of specific elements difficult. In addition, overlap between emission peaks of several elements and near-background fluorescence led to inaccurate representation of element distribution in fluorescence maps, which complicated data interpretation.

4.5. SR-XFM in the mining industry

In the mining industry, analytical techniques are mainly applied for routine quantitative analysis with a high sample throughput to monitor the ore feed and products (e.g., whole rock XRF, automated SEM, LIBS). Dedicated analyses on a smaller, yet statistically significant, number of samples may be performed for better characterisation of some minerals (e.g., EPMA, SIMS, LA-ICP-MS, µXRF). Accessibility to synchrotron facilities is limited and beam time constrained, making routine investigations hardly possible. Further, the number of samples analysed at a synchrotron facility are typically less than at a lab and the issues of sample representativeness and scalability, common in micro-analysis, even more pronounced. Achieving statistical significance, crucial in mining operations, is thus clearly challenging. Synchrotron radiation-based analysis is therefore mainly a research tool, well-suited to study ore forming processes and to address issues concerning metal recovery. Nevertheless, synchrotron radiation based-analysis should always be preceded by a thorough lab-based micro-analysis to guide sample selection and improve sample representativeness.

Two possible applications of SR-XFM in the mining industry were tested in this study. They rely on the combination of high spatial resolution (nanometre) and high detection range (sub-ppm): (1) Analysis of nano-inclusions: Inclusions of gangue in ore minerals can cause unwanted elements in the mineral concentrate and subsequently potentially also in the metal end-product. Vice versa, ore mineral inclusions in gangue can cause loss of metals to the tailings. SR-XFM may help to prove the existence of and characterise such inclusions, where lab-based methods lack in spatial resolution. This is particularly the case for submicron inclusions, as very few techniques demonstrate nanometre spatial resolution (Fig. 1). (2) Mapping of impurities at ppm-level: The distribution of impurities in some minerals (e.g., zoning) may reflect ore genetic conditions and knowledge thereof aid in ore deposit exploration. Further, it may explain inconsistent metal deportation during processing, e.g. due to distribution in the core versus along the margin of a grain. While many techniques offer ppm-level element mapping, the simultaneous nanometre spatial resolution and non-destructive nature is unique to SR-XFM (Fig. 1). If the superior resolution of SR-XFM to lab-based systems is of broader interest to the mining industry has yet to be assessed given the novelty of third- and fourth-generation synchrotron light sources. The results of this study indicated potential implications for metal recovery, but further analyses in combination with flotation tests are needed to evaluate their significance. Considering the continuous advancements in mineral processing, SR-XFM surely will find more application in the future. At the latest, once lab-based systems achieve nanometre resolution will studies at the nanoscale be common.

5. Conclusions

Synchrotron XFM is a powerful technique and proved effective for mapping of micro- to nanometre inclusions in molybdenite and pyrite. It also showed convincing results for ppm-element distribution mapping. Lattice-bound Re, W, and Se in molybdenite and zonation of As, Co, and Fe in pyrite were resolved. Mapping of a few-micrometre sized Bi grain highlighted the capabilities of extreme-resolution mapping. Nanometre-sized inclusions of several elements, including Au, within the Bi grain were resolved.

However, SR-XFM requires more careful planning, execution, and processing of data compared to many lab-based XRF technologies. Difficulties in accessing a synchrotron make SR-XFM inappropriate for routine investigations in the mining industry. However, for specific problems at hand for the industry (e.g., trace metal deportment during processing), SR-XFM may be an excellent tool. Dependency of data quality on the expertise of the user may further demotivate application of the synchrotron technology in the mining industry, unless post-processing of data can be supported and/or advised by the beamline scientists, which is typically the case. Nevertheless, the high resolution and low detection limits in a SR-XFM system are hardly obtainable by lab-based XRF systems. Synchrotron technology is therefore best suited to address specific issues that more accessible techniques fail to solve, e.g. if metal deportment is impacted by nano-inclusions and the distribution pattern of impurities. With constant development in mineral processing and metallurgy, unravelling the complexity of ore minerals at the nanoscale may prove especially valuable to improving metal recovery. Synchrotron XFM is well suited for this task. Results of this study showed particular strength in the combination of nanometre resolution with ppm detection levels. Yet, they also showed that SR-XFM is best applied in conjunction with other techniques like SEM-EDS, EPMA, or LA-ICP-MS.

Declaration of Competing Interest

The authors declare that they have no known competing financial interests or personal relationships that could have appeared to influence the work reported in this paper.

Acknowledgements

Dr. Franco Pirajno is thanked for constructive editorial work, and three anonymous reviewers significantly improved the manuscript. The authors would also like to thank the staff at the MAX IV synchrotron facility in Lund, Sweden, for excellent support during analytical work. This study was funded by Sweden's Innovation Agency (project 2018-04426; Nano-scale characterization of ore minerals for an optimized metal extraction process (NanoORE)) and the Center of Advanced Mining and Metallurgy (CAMM) at Luleå University of Technology, together with Boliden Mineral AB.

References

Adams, F. (2010). Synchrotron X-ray fluorescence analysis in environmental and earth sciences. In: *EPJ Web of* Conferences (Vol. 9, p. 165-180). EDP Sciences. doi: 10.1051/epjconf/201009013.

Aleinikoff, J.N., Creaser, R.A., Lowers, H.A., Magee Jr, C.W., Grauch, R.I., 2012. Multiple age components in individual molybdenite grains. Chem. Geol. 300, 55–60. https://doi.org/10.1016/j.chemgeo.2012.01.011.

Ametov, I., Grano, S., Zanin, M., Gredelj, S., Magnuson, R., Bolles, T., & Triffett, B. (2008). Copper and molybdenite recovery in plant and batch laboratory cells in porphyry copper rougher flotation. In: *W.F. Liang (ed.): Proceedings of the 24th International Mineral Processing Congress*, Beijing, China, 24-28 September 2008, 141, 1129-1137. Science Press.

Arehart, G.B., Chryssoulis, S.L., Kesler, S.E., 1993. Gold and arsenic in iron sulfides from sediment-hosted disseminated gold deposits; implications for depositional processes. Econ. Geol. 88 (1), 171–185. https://doi.org/10.2113/gsecongeo.88.1.171.

Belcher, R.W., Rozendaal, A., Przybylowicz, W.J., 2004. Trace element zoning in pyrite determined by PIXE elemental mapping: evidence for varying ore–fluid composition and electrochemical precipitation of gold at the Spitskop deposit, Saldania Belt, South Africa. X-Ray Spectrom.: An Int. J. 33 (3), 174–180. https://doi.org/10.1002/xrs.680.

Benavente, E., Santa Ana, M.A., Mendizábal, F., González, G., 2002. Intercalation chemistry of molybdenum disulfide. Coord. Chem. Rev. 224 (1–2), 87–109. https://doi.org/10.1016/S0010-8545(01)00392-7.

Björling, A., Kalbfleisch, S., Kahnt, M., Sala, S., Parfeniukas, K., Vogt, U., Carbone, D., Johansson, U., 2020. Ptychographic characterization of a coherent nanofocused X-ray beam. Opt. Express 28 (4), 5069–5076. https://doi.org/10.1364/OE.386068.

Brugger, J., Pring, A., Reith, F., Ryan, C., Etschmann, B., Liu, W., O'Neil, B., Ngothai, Y., 2010. Probing ore deposits formation: New insights and challenges from synchrotron and neutron studies. Radiat. Phys. Chem. 79 (2), 151–161. https://doi.org/10.1016/j.radphyschem.2009.03.071.

Čech, F., Rieder, M., Vrána, S., 1973. Drysdallite, MoSe 2, a new mineral. Neues Jahrbuch für Mineralogie, Monatshefte 10, 433–442.

Chander, S., Fuerstenau, D.W., 1972. On the natural floatability of molybdenite. Trans. AIME 252, 62–69.

Ciobanu, C.L., Cook, N.J., July 2002. (2002). Tellurides, selenides (and bi-sulphosalts) in gold deposits. In: Robb, L.J., Montjoie, R. (Eds.), Abstract Volume of the 11th quadrennial IAGOD symposium and Geocongress. Namibia, Windhoek, pp. 22–26.

Ciobanu, C.L., Cook, N.J., Pring, A., Brugger, J., Danyushevsky, L.V., Shimizu, M., 2009. 'Invisible gold' in bismuth chalcogenides. Geochim. Cosmochim. Acta 73 (7), 1970–1999. https://doi.org/10.1016/j.gca.2009.01.006.

Ciobanu, C.L., Cook, N.J., Kelson, C.R., Guerin, R., Kalleske, N., Danyushevsky, L., 2013. Trace element heterogeneity in molybdenite fingerprints stages of mineralization. Chem. Geol. 347, 175–189. https://doi.org/10.1016/j.chemgeo.2013.03.011.

Coetzee, L.L., Theron, S.J., Martin, G.J., Van der Merwe, J.D., Stanek, T.A., 2011. Modern gold deportments and its application to industry. Miner. Eng. 24 (6), 565–575. https://doi.org/10.1016/j.mineng.2010.09.001.

Cook, N.J., Chryssoulis, S.L., 1990. Concentrations of invisible gold in the common sulfides. The Canadian Mineralogist 28 (1), 1–16.

Cook, N.J., Ciobanu, C.L., 2005. Tellurides in Au deposits: implications for modelling. In: Mao, J., Bierlein, F.P. (Eds.), Mineral deposit research: meeting the global challenge. Springer, Berlin, Heidelberg, pp. 1387–1390. https://doi.org/10.1007/3-540-27946-6_353.

Cook, N.J., Ciobanu, C.L., Spry, P.G., Voudouris, P., 2009. Understanding gold-(silver)-telluride-(selenide) mineral deposits. Episodes 32 (4), 249–263. https://doi.org/10.18814/epiiugs/2009/v32i4/002.

Cook, N.J., Ciobanu, C.L., Ehrig, K., Slattery, A., Verdugo-Ihl, M.R., Courtney-Davies, L., Gao, W., 2017. Advances and opportunities in ore mineralogy. Minerals 7 (12), 233. https://doi.org/10.3390/min7120233.

Craig, J.R., Vokes, F.M., Solberg, T.N., 1998. Pyrite: physical and chemical textures. Miner. Deposita 34 (1), 82–101. https://doi.org/10.1007/s001260050187.

Dippenaar, A., 1982. The destabilization of froth by solids. I. The mechanism of film rupture. Int. J. Miner. Process. 9 (1), 1–14. https://doi.org/10.1016/0301-7516(82)90002-3.

Douglas, N., Mavrogenes, J., Hack, A. & England, R., (2000). The liquid bismuth collector model: an alternative gold deposition mechanism. In: *C.G. Skillbeck & T.C. T. Hubble (eds.): Searching for a sustainable future: 15th Australian Geological Convention*, Sydney, Australia, 3-7 July 2000, 135 pp.

Drábek, M., 1995. The Mo-Se-S and the Mo-Te-S systems. Neues Jahrbuch für Mineralogie-Abhandlungen 169 (3), 255–263.

Eggert, R.G. (Ed.). (1994). *Mining and the environment: international perspectives on public policy*. Resources for the Future.

Etschmann, B., Liu, W., Li, K., Dai, S., Reith, F., Falconer, D., Kerr, G., Paterson, D., Howard, D., Kappen, P., Wykes, J., Brugger, J., 2017. Enrichment of germanium and associated arsenic and tungsten in coal and roll-front uranium deposits. Chem. Geol. 463, 29–49. https://doi.org/10.1016/j.chemgeo.2017.05.006.

Fisher, L.A., Fougerouse, D., Cleverley, J.S., Ryan, C.G., Micklethwaite, S., Halfpenny, A., Hough, R.M., Gee, M., Paterson, D., Howard, D.L., Spiers, K., 2015. Quantified, multi-scale X-ray fluorescence element mapping using the Maia detector array: Application to mineral deposit studies. Miner. Deposita 50 (6), 665–674. https://doi.org/10.1007/s00126-014-0562-z.

Fleet, M.E., 1989. Oscillatory-zoned As-bearing pyrite from strata-bound and stratiform gold deposits: an indicator of ore fluid evolution. Economic Geology Monograph 6, 356–362.

Fleet, M.E., Chryssoulis, S.L., MacLean, P.J., Davidson, R., Weisener, C.G., 1993. Arsenian pyrite from gold deposits; Au and As distribution investigated by SIMS and EMP, and color staining and surface oxidation by XPS and LIMS. The Canadian Mineralogist 31 (1), 1–17.

Fleischer, M., 1959. The geochemistry of rhenium, with special reference to its occurrence in molybdenite. Econ. Geol. 54 (8), 1406–1413. https://doi.org/10.2113/gsecongeo.54.8.1406.

Frondel, J.W., Wickman, F.E., 1970. Molybdenite polytypes in theory and occurrence. II. Some naturally-occurring polytypes of molybdenite. American Mineralogist: Journal of Earth and Planetary Materials 55 (11–12), 1857–1875.

Golden, J., McMillan, M., Downs, R.T., Hystad, G., Goldstein, I., Stein, H.J., Zimmermann, A., Sverjensky, D.A., Armstrong, J.T., Hazen, R.M., 2013. Rhenium variations in molybdenite (MoS2): Evidence for progressive subsurface oxidation. Earth Planet. Sci. Lett. 366, 1–5. https://doi.org/10.1016/j.epsl.2013.01.034.

Grabezhev, A.I., Voudouris, P.C., 2014. Rhenium distribution in molybdenite from the Vosnesensk porphyry Cu±(Mo, Au) deposit (southern Urals, Russia). The Canadian Mineralogist 52 (4), 671–686. https://doi.org/10.3749/canmin.1300048.

Harris, D.C., 1990. The mineralogy of gold and its relevance to gold recoveries. Miner. Deposita 25 (1), 3–7.

Hoover, M.R., 1980. Water Chemistry Effects in the Flotation of Sulfide Ores - a Review and Discussion for Molybdenite. Complex Sulphide Ores 100–112.

Hu, S.Y., Evans, K., Fisher, L., Rempel, K., Craw, D., Evans, N.J., Cumberland, S., Robert, A., Grice, K., 2016. Associations between sulfides, carbonaceous material, gold and other trace elements in polyframboids: implications for the source of orogenic gold deposits, Otago Schist, New Zealand. Geochim. Cosmochim. Acta 180, 197–213. https://doi.org/10.1016/j.gca.2016.02.021.

European Commission (2020). Study on the EU's list of Critical Raw Materials (2020). doi: https://doi.org/10.2873/11619.

Johansson, U., Vogt, U., & Mikkelsen, A. (2013). NanoMAX: a hard x-ray nanoprobe beamline at MAX IV. In *X-Ray Nanoimaging: Instruments and Methods* (Vol. 8851, p. 88510L). International Society for Optics and Photonics. doi:10.1117/12.2026609.

Kropschot, S.J., 2009. Molybdenum-A Key Component of Metal Alloys. USGS Mineral Resources Program, Fact Sheet 2009-3106. https://doi.org/10.3133/fs20093106.

Li, K., Etschmann, B., Rae, N., Reith, F., Ryan, C.G., Kirkham, R., Howard, D., Rosa, D.R. N., Zammit, C., Pring, A., Ngothai, Y., Hooker, A., Brugger, J., 2016. Ore petrography using megapixel X-ray imaging: rapid insights into element distribution and mobilization in complex Pt and U-Ge-Cu ores. Econ. Geol. 111 (2), 487–501. https://doi.org/10.2113/econgeo.111.2.487.

Lintern, M.J., Hough, R.M., Ryan, C.G., Watling, J., Verrall, M., 2009. Ionic gold in calcrete revealed by LA-ICP-MS, SXRF and XANES. Geochim. Cosmochim. Acta 73 (6), 1666–1683. https://doi.org/10.1016/j.gca.2008.12.019.

Pals, D.W., Spry, P.G., Chryssoulis, S., 2003. Invisible gold and tellurium in arsenic-rich pyrite from the Emperor gold deposit, Fiji: implications for gold distribution and deposition. Econ. Geol. 98 (3), 479–493. https://doi.org/10.2113/gsecongeo.98.3.479.

Majumdar, S., Peralta-Videa, J.R., Castillo-Michel, H., Hong, J., Rico, C.M., Gardea-Torresdey, J.L., 2012. Applications of synchrotron μ-XRF to study the distribution of biologically important elements in different environmental matrices: A review. Anal. Chim. Acta 755, 1–16. https://doi.org/10.1016/j.aca.2012.09.050.

McClung, C.R., 2016. Molybdenite polytypism and its implications for processing and recovery: A geometallurgical-based case study from Bingham Canyon Mine, Utah. *Miner. Metall. Process.* 33 (3), 149–154. https://doi.org/10.19150/mmp.6752.

Millensifer, T.A., Sinclair, D., Jonasson, I., Lipmann, A., 2014. Rhenium. Crit. Metals Handbook 340–360.

Pašava, J., Svojtka, M., Veselovský, F., Ďurišová, J., Ackerman, L., Pour, O., Drábek, M., Halodová, P., Haluzová, E., 2016. Laser ablation ICPMS study of trace element chemistry in molybdenite coupled with scanning electron microscopy (SEM)—an important tool for identification of different types of mineralization. Ore Geol. Rev. 72, 874–895. https://doi.org/10.1016/j.oregeorev.2015.09.007.

Raghavan, S., Hsu, L.L., 1984. Factors affecting the flotation recovery of molybdenite from porphyry copper ores. Int. J. Miner. Process. 12 (1–3), 145–162. https://doi.org/10.1016/0301-7516(84)90026-7.

Ren, Z., Zhou, T., Hollings, P., White, N.C., Wang, F., Yuan, F., 2018. Trace element geochemistry of molybdenite from the Shapinggou super-large porphyry Mo deposit, China. Ore Geol. Rev. 95, 1049–1065. https://doi.org/10.1016/j.oregeorev.2018.02.011.

Ryan, C.G., Clayton, E., Griffin, W.L., Sie, S.H., Cousens, D.R., 1988. SNIP, a statistics-sensitive background treatment for the quantitative analysis of PIXE spectra in geoscience applications. Nucl. Instrum. Methods Phys. Res., Sect. B 34 (3), 396–402. https://doi.org/10.1016/0168-583X(88)90063-8.

Ryan, C. G., Siddons, D. P., Kirkham, R., Li, Z. Y., De Jonge, M. D., Paterson, D., Cleverley, J. S., Kuczewski, A., Dunn, P. A., Jensen, M., De Geronimo, G., Howard, D. L., Godel, B., Dyl, K. A., Fisher, L. A., Hough, R. H., Barnes, S. J., Bland, P. A., Moorhead, G., James, S. A., Spiers, K. M., Falkenberg, G., Boesenberg, U., & Wellenreuther, G. (2013). The Maia detector array and X-ray fluorescence imaging system: locating rare precious metal phases in complex samples. In *X-Ray Nanoimaging: Instruments and Methods* (Vol. 8851, p. 88510Q). International Society for Optics and Photonics. doi:10.1117/12.2027195.

Sammelin, M., Wanhainen, C., Martinsson, O., 2011. Gold mineralogy at the Aitik Cu–Au–Ag deposit, Gällivare area, northern Sweden. GFF 133 (1–2), 19–30. https://doi.org/10.1080/11035897.2010.551542.

Smith, J.V., 1995. Tutorial review. synchrotron x-ray sources: instrumental characteristics. new applications in microanalysis, tomography, absorption spectroscopy and diffraction. Analyst 120 (5), 1231–1245. https://doi.org/10.1039/AN9952001231.

Solé, V.A., Papillon, E., Cotte, M., Walter, P., Susini, J.A., 2007. A multiplatform code for the analysis of energy-dispersive X-ray fluorescence spectra. Spectrochim. Acta, Part B 62 (1), 63–68. https://doi.org/10.1016/j.sab.2006.12.002.

Stein, H.J., 1998. An introduction to Re-Os: What's in it for the mineral industry. SEG Newsletter 32, 1–8.

Stein, H.J., Markey, R.J., Morgan, J.W., Hannah, J.L., Scherstén, A., 2001. The remarkable Re–Os chronometer in molybdenite: how and why it works. Terra Nova 13 (6), 479–486. https://doi.org/10.1046/j.1365-3121.2001.00395.x.

Stein, H., Scherstén, A., Hannah, J., Markey, R., 2003. Subgrain-scale decoupling of Re and 187Os and assessment of laser ablation ICP-MS spot dating in molybdenite. Geochim. Cosmochim. Acta 67 (19), 3673–3686. https://doi.org/10.1016/S0016-7037(03)00269-2.

Stromberg, J.M., Van Loon, L.L., Gordon, R., Woll, A., Feng, R., Schumann, D., Banerjee, N.R., 2019. Applications of synchrotron X-ray techniques to orogenic gold studies; examples from the Timmins gold camp. Ore Geol. Rev. 104, 589–602. https://doi.org/10.1016/j.oregeorev.2018.11.015.

Terada, K., Osaki, S., Ishihara, S., Kiba, T., 1971. Distribution of rhenium in molybdenites from Japan. Geochem. J. 4 (3), 123–141. https://doi.org/10.2343/geochemj.4.123.

Tooth, B., Brugger, J., Ciobanu, C., Liu, W., 2008. Modeling of gold scavenging by bismuth melts coexisting with hydrothermal fluids. Geology 36 (10), 815–818. https://doi.org/10.1130/G25093A.1.

Tooth, B., Ciobanu, C.L., Green, L., O'Neill, B., Brugger, J., 2011. Bi-melt formation and gold scavenging from hydrothermal fluids: an experimental study. Geochim. Cosmochim. Acta 75 (19), 5423–5443. https://doi.org/10.1016/j.gca.2011.07.020.

Triffett, B., Veloo, C., Adair, B.J.I., Bradshaw, D., 2008. An investigation of the factors affecting the recovery of molybdenite in the Kennecott Utah Copper bulk flotation circuit. Miner. Eng. 21 (12–14), 832–840. https://doi.org/10.1016/j.mineng.2008.03.003.

U.S. National Research Council, 2008. Minerals, critical minerals, and the US economy. National Academies Press.

Vaughan, J.P., 2004. The process mineralogy of gold: the classification of ore types. JOM 56 (7), 46–48. https://doi.org/10.1007/s11837-004-0092-8.

Von der Heyden, B.P., 2020. Shedding light on ore deposits: A review of synchrotron X-ray radiation use in ore geology research. Ore Geol. Rev. 117, 103328 https://doi.org/10.1016/j.oregeorev.2020.103328.

Wagner, T., 2007: Thermodynamic modeling of Au–Bi–Te melt precipitation from high temperature hydrothermal fluids: preliminary results. In *C.J. Andrew (ed.): Mineral Exploration and Research: Digging Deeper. Proceedings of the 9th Biennial SGA Meeting*, Dublin, Ireland, 20–23 August 2007, 769–772.

Wanhainen, C., Nigatu, W., Selby, D., McLeod, C.L., Nordin, R., Bolin, N.J., 2014. The distribution, character, and rhenium content of molybdenite in the Aitik Cu-Au-Ag-(Mo) deposit and its southern extension in the northern Norrbotten ore district, northern Sweden. Minerals 4 (4), 788–814. https://doi.org/10.3390/min4040788.

Warlo, M., Wanhainen, C., Bark, G., Karlsson, P., 2019. Gold and Silver Mineralogy of the Liikavaara Cu-(W-Au) Deposit, Northern Sweden. *Proceedings of the 15th SGA Biennial Meeting*.

Warlo, M., Wanhainen, C., Martinsson, O., Karlsson, P., 2020. Mineralogy and character of the Liikavaara Östra Cu-(W-Au) deposit, northern Sweden. GFF 142 (3), 1–21. https://doi.org/10.1080/11035897.2020.1753807.

Wells, J.D., Mullens, T.E., 1973. Gold-bearing arsenian pyrite determined by microprobe analysis, Cortez and Carlin gold mines, Nevada. *Econ. Geol.* 68 (2), 187–201. https://doi.org/10.2113/gsecongeo.68.2.187.

Woodcock, J.T., Sparrow, G.J., Bruckard, W.J., 2007. Flotation of Precious Metals and Their Minerals. In: Fuerstenau, M.C., Jameson, G., Yoon, R.-.H. (Eds.), *Froth Flotation: A Century of Innovation*, 575–609. SME, Littleton.

Wu, Y.F., Fougerouse, D., Evans, K., Reddy, S.M., Saxey, D.W., Guagliardo, P., Li, J.W., 2019. Gold, arsenic, and copper zoning in pyrite: A record of fluid chemistry and growth kinetics. Geology 47 (7), 641–644. https://doi.org/10.1130/G46114.1.

Zanin, M., Gredelj, S., Grano, S., 2008. Factors affecting froth stability in mineral flotation and implications on minerals recovery: A case of study. In: Casali, A., Gómez, C., Kuyvenhoven, R. (Eds.), PROCEMIN 2008 - V International Mineral Processing Seminar. Santiago, Chile, pp. 197–206.

Zanin, M., Ametov, I., Grano, S., Zhou, L., Skinner, W., 2009. A study of mechanisms affecting molybdenite recovery in a bulk copper/molybdenum flotation circuit. Int. J. Miner. Process. 93 (3–4), 256–266. https://doi.org/10.1016/j.minpro.2009.10.001.

Zweifel, H., 1976. Aitik – geological documentation of a disseminated copper deposit: a preliminary investigation. Sveriges Geologiska Undersökning C 720, 80.

Zhou, J.Y., Cabri, L.J., 2004. Gold process mineralogy: Objectives, techniques, and applications. JOM 56 (7), 49–52. https://doi.org/10.1007/s11837-004-0093-7.